Model-based observer and feedback control design for a rigid Joukowski foil in a Kármán vortex street

Brian A. Free and Derek A. Paley

Department of Aerospace Engineering and Institute for Systems Research, University of Maryland, College Park, MD 20742, USA

E-mail: bfree@umd.edu, dpaley@umd.edu

Abstract. Obstacles and swimming fish in flow create a wake with an alternating left/right vortex pattern known as a Kármán vortex street and reverse Kármán vortex street, respectively. An energy-efficient fish behavior resembling slaloming through the vortex street is called Kármán gaiting. This paper describes the use of a bioinspired array of pressure sensors on a Joukowski foil to estimate and control flow-relative position in a Kármán vortex street using potential flow theory, recursive Bayesian filtering, and trajectory-tracking feedback control. The Joukowski foil is fixed in downstream position in a flowing water channel and free to move on air bearings in the cross-stream direction by controlling its angle of attack to generate lift. Inspired by the lateral-line neuromasts found in fish, the sensing and control scheme is validated using off-the-shelf pressure sensors in an experimental testbed that includes a flapping device to create vortices. We derive a potential flow model that describes the flow over a Joukowski foil in a Kármán vortex street and identify an optimal path through a Kármán vortex street using empirical observability. The optimally observable trajectory is one that passes through each vortex in the street. The estimated vorticity and location of the Kármán vortex street are used in a closed-loop control to track either the optimally observable path or the energetically efficient gait exhibited by fish. Results from the closed-loop control experiments in the flow tank show that the artificial lateral line in conjunction with a potential flow model and Bayesian estimator allow the robot to perform fish-like slaloming behavior in a Kármán vortex street. This work is a precursor to an autonomous robotic fish sensing the wake of another fish and/or performing pursuit and schooling behavior.

Keywords: flow sensing, closed-loop control, bioinspiration, vortex street, Bayesian estimation, fish swimming

1. Introduction

Autonomous navigation of underwater vehicles through complex flow structures such as the turbulent wake of another vehicle requires a sensing mechanism to perceive variable flow patterns. Fish have a sensing structure known as the lateral line, which contains spatially distributed superficial and canal neuromasts sensitive to flow velocity and pressure gradients respectively [1,2], that provides inspiration for a similar sensing system for underwater vehicles. Fish utilize lateral-line sensing of the hydrodynamic properties of the flow to help navigate and seek prey, even in complete darkness [3–5]. Bioinspired artificial lateral lines comprised of pressure sensors have the potential to enable robotic platforms to estimate the flow speed and angle of attack in uniform flows [6] and the location and strength of circulating flow structures such as vortices and vortex streets [7].

A frequently studied circulating structure is the Kármán vortex street, a pattern of clockwise and anti-clockwise vortices shed by a blunt body due to flow separation [8]. This pattern is also produced in the wake of fish as they swim (though with opposite vortex strength, known as a reverse Kármán vortex street) [9], and is investigated here as a precursor to fish-robot multi-vehicle control including pursuit and schooling behavior.

This work describes the use of a Bayesian filter in conjunction with a potential flow model and distributed pressure sensors on a fish-shaped, underwater Joukowski foil [10, 11] to estimate the strength, phase, and cross-stream location of a Kármán vortex street, as well as the design of a feedback controller to drive the foil to an arbitrary reference trajectory through the street. The Joukowski foil is fixed in its downstream position in a flow tank and its angle of attack is controlled so the foil moves in the cross-stream direction along an air-bearing track. It can be programmed to follow any differentiable reference trajectory through a vortex street. Particularly, an optimal sinusoidal path determined by empirical observability and the slaloming path known as Kármán gaiting are experimentally validated. Observability is a concept that determines how well a set of states can be reproduced from a set of measurements, if at all.

Fish in nature slalom through alternating vortices using a combination of their lateral line and vision system and are capable of Kármán gaiting even in the absence of vision [12]. Research has also shown that during Kármán gaiting behavior the tail-beat frequency of the fish matches the vortex-shedding frequency and muscle activity decreases compared to station holding in uniform flow [13]. Dead (but still flexible) trout towed behind an obstacle in the flow can even exhibit Kármán gaiting and passively generate thrust [14].

The lateral line in fish is an important sensing mechanism for navigating the underwater space, particularly for Kármán gaiting, but also for schooling [15], predator/prey detection [16, 17], and wall following [4]. The effective sensing range of the lateral line is on the order of one body length [18]. An artificial lateral line has the capability of providing the same sensing mechanism to robotic fish and marine vessels. The signal on the nerve fibers in fish associated with the lateral line carries enough information to determine the vortex-shedding frequency of a Kármán vortex street and can also be decoded to locate the source of a vibrating dipole [19, 20].

In prior work on an artificial lateral line, Yang et al. showed that a MEMS-based lateral line was capable of localizing a vibrating dipole [21]. Gao and Triantafyllou further describe sensing and controlling the yaw of a robotic underwater vehicle equipped with an artificial lateral line composed of pressure sensors [22]. Lagor et al. equipped a Joukowski foil with commercial pressure sensors to estimate angle of attack and flow speed in uniform flow and used the estimate in a closed-loop control to demonstrate rheotaxis [6]. DeVries et al. used pressure sensors with ionic polymer-metal composites (IPMC) velocity sensors in a bi-modal artificial lateral line to estimate the location of an upstream obstacle and performed station holding behind the obstacle using feedback control [23]. Lagor et al. determined the best path of an underwater glider to tour an ocean-scale, two-vortex system using the local unobservability index [24].

There is a large body of work on artificial lateral lines used as a sensing mechanism to detect vortices or estimate associated parameters. Li and Saimek estimated the strength of free vortices in the flow with pressure sensors distributed on an underwater foil and a Kalman filter [25]. Fernandez used pressure sensors on a flat plate as well as a streamlined body to estimate the location of moving vortices, but performed no closed-loop control [26]. In simulation, Ren and

Mohseni show that the lateral line sensing carries enough information to determine all parameters of the potential flow model of a vortex street by modeling the lateral line as an infinite flat plate and performing a numerical approximation to the flow over a Joukowski airfoil [27]. Salumäe and Kruusmaa created a fish robot capable of detecting whether or not it is in a Kármán vortex street using an artificial lateral line and navigating to the turbulent wake, but the authors did not provide an analytical model for the flow or an estimate of vortex positions within the street [28]. In a similar vein, Venturelli et al. demonstrate that an artificial lateral line can be used to distinguish uniform flow from a Kármán vortex street, as well as the vortex-shedding frequency, travelling speed, and downstream vortex spacing [29]. Using an artificial lateral line comprised of optical flow sensors, Klein and Bleckmann localize a cylinder producing a Kármán vortex street by comparing the time history of the distributed sensors, but provide no estimate of the position of vortices within the street and perform no closed-loop control [30]. Most recently, Wang et al. equipped a robotic fish with an artificial lateral line and were able to determine the swimming frequency and distance to an upstream robotic fish that was shedding a reverse Kármán vortex street, but did not investigate the case where the robot was not colinear with the vortex street [31].

In our previous work [7], pressure sensors were used to estimate the state of a vortex street and demonstrate closed-loop control to an optimally observable reference trajectory, but there was no Joukowski foil in the flow and the sensor array position was controlled directly through a stepper motor. The optimally observable trajectory was a sinusoidal path 180° out of phase from Kármán gaiting behavior, meaning that the sensor array was to collide with each vortex in the street. A Bayesian filter using a potential flow model of a Kármán vortex street estimated the strength, phase, and cross-stream position of the street relative to the sensor array.

This paper, building on our previous work [7], aims to use feedback control to track reference trajectories through a Kármán vortex street. This aim requires an estimate of the location of vortices within the street, represented by the estimated phase and cross-stream location of the street. This fish-inspired behavior has applications in pursuit and schooling behavior of autonomous underwater vehicles. The optimally observable path may be desirable for platforms with larger sensor noise or where certainty in the estimate is of prime importance. Kármán gaiting may be desirable in cases where energy conservation is important. Matching the tail-beat frequency of a robotic fish to the vortex shedding frequency has shown to increase swimming efficiency [32]. This work does not investigate the efficiency of the biological Kármán gaiting trajectory, but develops the necessary tools to follow it.

A model free approach [21, 28–31] relies on examining the data from an artificial lateral line and establishing heuristic methods to determine various parameters of a vortex street. The analytical model developed herein is independent of the shape of the Joukowski foil and sensor placement so it is easily adaptable to a variety of platforms, whereas a model-free approach requires new heuristics for each sensor or body configuration.

The methodology of this work is outlined below and uses tools from potential flow theory, nonlinear estimation, and nonlinear observability. Estimates of the strength, phase, and cross-stream location of a vortex street are formed using pressure measurements from an artificial lateral line and used in closed-loop, trajectory-tracking feedback control. The Kármán vortex street is modeled as a potential flow with two parallel infinite lines of vortices [8]. The Joukowski foil is placed in the flow model using the Joukowski transformation on a cylinder [10] and the Milne-Thomson Circle Theorem [33]. Measurement equations formed with the potential flow model and Bernoulli's principle output the predicted pressure reading according to three states (vortex strength of the street, cross-stream position of the street, and a phase angle that represents the downstream position of the primary vortex in the street). In line with the goal of a fully autonomous vehicle, all parameters and calculations are in a reference frame fixed to the Joukowski foil. The measurement equations, in conjunction with real-time sensor readings, are used in a nonlinear, recursive, grid-based Bayesian framework to estimate the three states. The estimate is used in feedback control of the angle of attack of the Joukowski foil to generate lift in the cross-stream direction and to track a reference trajectory through the street.

The techniques developed in this paper are demonstrated in an experimental testbed. The testbed includes a 185 L flow tank, an air-bearing system to allow movement of the Joukowski foil in the cross-stream direction, and a system to generate vortices in the desired Kármán vortex street pattern. The system was successful in estimating the state of the vortex street as well as tracking the reference trajectories. This work has applications in autonomous underwater navigation in cluttered environments and sensing or pursuing other fish or robots in water.

The contributions of this paper are (1) a potential flow model of the flow over an airfoil in a Kármán vortex street including a solution to the Kutta condition, which guarantees flow leaves smoothly at the

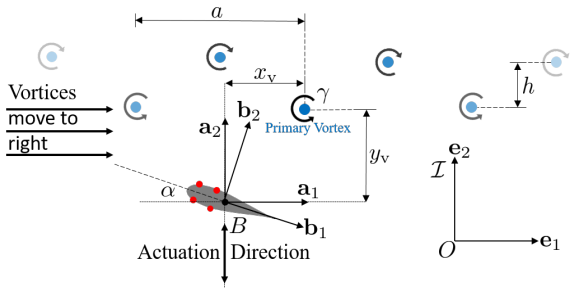

Figure 1. Illustration of sensor and control system for the Kármán vortex street. Red circles are pressure sensors.

trailing edge of the foil and (2) closed-loop feedback control of a Joukowski foil with an artificial lateral line along an arbitrary trajectory using angle of attack regulation to produce lift in the flow. Additionally, we extend the results of our previous work [7] by deriving a new potential flow model that includes a foil in the flow. With this extension, we present here a Bayesian filter framework using pressure measurements to estimate the vortex strength, location, and phase of a Kármán vortex street as well as the calculation of an optimally observable path through a vortex street based on empirical observability, which yields a sinusoidal path 180° out of phase from Kármán gaiting behavior.

The paper proceeds as follows. Section 2 presents the model for the flow over a Joukowski airfoil subject to a Kármán vortex street and derives the measurement equation for the artificial lateral line. Section 3 describes the Bayesian framework used to estimate the location and strength of the vortex street. Section 4 covers the dynamics of the Joukowski foil and the controller for the angle of attack of the Joukowski foil. Section 5 presents the work on empirical observability-based path planning. Section 6 describes results from the experimental demonstration and Section 7 summarizes the paper and ongoing work.

2. Modeling flow over a Joukowski airfoil in a Kármán vortex street

Figure 1 shows the physical layout of the modeling framework and the goal of the sensing and control design below. The Joukowski foil has four pressure sensors distributed on the forefront of the body. The Kármán vortex street is modeled with potential flow theory. The inertial reference frame $\mathcal{I} = (O, \mathbf{e}_1, \mathbf{e}_2)$ is aligned such that $\mathbf{e}_1 = \mathbf{a}_1$ is pointing downstream. The body-fixed, non-rotating frame $\mathcal{A} = (B, \mathbf{a}_1, \mathbf{a}_2)$ is aligned with $\mathcal{I}$ and centered on the origin of the Joukowski foil. The body-fixed frame $\mathcal{B} = (B, \mathbf{b}_1, \mathbf{b}_2)$ is aligned with $\mathbf{b}_1$ pointing to the tail of the Joukowski foil and is rotated from frame $\mathcal{A}$ by the angle of attack α. The closest anti-clockwise vortex to the Joukowski foil, i.e., the primary vortex, has coordinates $z_v = x_v\mathbf{e_1} + y_v\mathbf{e_2} = x_v + \mathbf{j}y_v$ in frame $\mathcal{A}$, where $\mathbf{j} = \sqrt{-1}$ is the imaginary number. Each vortex has strength γ or $-\gamma$ and the vortex street moves to the right with speed U. Every like-signed vortex in the street is spaced horizontally by a units. The two lines of vortices are separated vertically by h units. The Joukowski foil is fixed in the $\mathbf{a}_1$ direction and actuates in the $\mathbf{a}_2$ direction by controlling its angle of attack α to generate lift.

The Joukowski foil shape of the robot allows the use of a potential flow model. A potential flow model produces the flow velocity at any point from the derivative of a scalar potential function [10, 33, 34]. Potential flow theory characterizes invisid, irrotational, incompressible flows at low speed flows where viscous effects are minimal. Though the flow may separate at large angles of attack, the pressure sensors are grouped towards the head of the Joukowski foil where the flow is attached and the model remains valid [10]. Section 2.1 presents the flow over a cylinder at a non-zero angle of attack and the corresponding flow induced by a Kármán vortex street. An altered version of the Milne-Thomson Circle Theorem maintains the cylinder as a boundary condition. Section 2.2 presents the Joukowski transformation that converts flow past a cylinder to flow past an airfoil and derives the condition on the circulation around the cylinder to maintain the Kutta condition. Section 2.3 uses Bernoulli's equation to derive the measurement equation that gives the pressure difference between two sensors in the artificial lateral line as a function of the three states of the vortex street.

Figure 2 shows the flow in the pre-transform ζ-plane and in the post-transform z-plane, in which the cylinder is transformed into an airfoil. Note that the vortices are in a straight line only in the ζ-plane; the Joukowski transformation has an unintended effect of shifting the position of vortices near the cylinder.

2.1. Flow in the ζ-plane

Modeling flow around a cylinder is a well known application of potential flow theory. The potential flow $F_C(\zeta)$ around a cylinder centered at location ζ_0 in the complex plane is modeled as the summation of uniform flow, a doublet, and a vortex [10]:

$$F_C(\zeta) = U(\zeta - \zeta_0)e^{-\mathbf{j}\alpha} + \frac{Ur_0^2}{\zeta - \zeta_0}e^{\mathbf{j}\alpha} - \mathbf{j}\frac{\Gamma_C}{2\pi}\ln\left(\frac{\zeta - \zeta_0}{r_0}\right), \quad (1)$$

where U is the flow speed, α is the angle of attack, r_0 is the radius of the cylinder, and Γ_C is the circulation strength. In potential flow, the velocity field of a potential flow $f(z)$ is given by the complex conjugate of the derivative of the potential $f(z)$ [10], i.e.,

$$w(z) = u(z) - \mathbf{j}v(z) = \frac{\mathrm{d}f}{\mathrm{d}z},$$

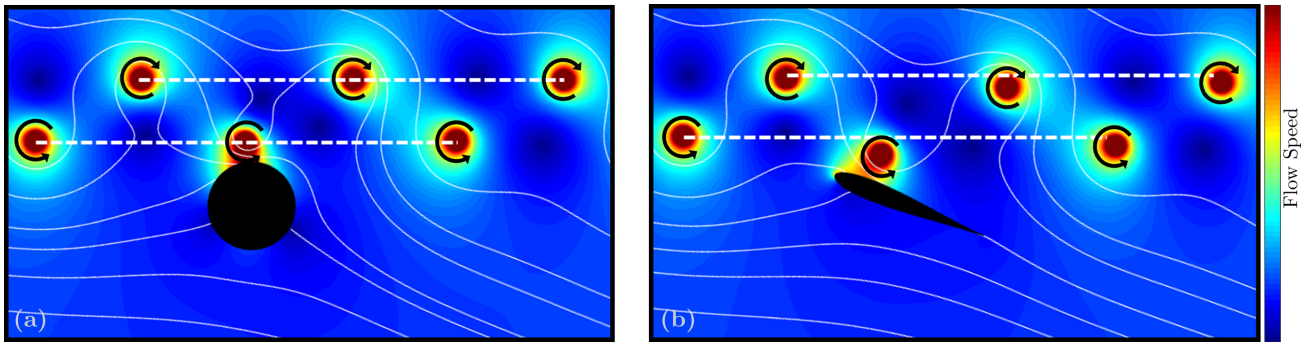

Figure 2. Simulated flow field of a lifting cylinder near a Kármán vortex street (a) in the ζ-plane and (b) in the transformed z-plane.

where $u(z)$ and $v(z)$ are the horizontal and vertical components of the velocity. The true velocity field is found by taking the complex conjugate, $\overline{w(z)} = u(z) + \mathbf{j}v(z)$. The conjugate velocity field for the lifting cylinder in the ζ-plane is

$$\frac{\mathrm{d}F_{\mathrm{C}}}{\mathrm{d}\zeta} = Ue^{-\mathbf{j}\alpha} - U\left(\frac{r_0}{\zeta-\zeta_0}\right)^2 e^{\mathbf{j}\alpha} - \mathbf{j}\frac{\Gamma_{\mathrm{C}}}{2\pi}\frac{1}{\zeta-\zeta_0}. \tag{2}$$

From [8], the potential function for a Kármán vortex street is

$$F_{\mathrm{K}}(\zeta) = \mathbf{j}\frac{\gamma}{2\pi}\left[\log\sin\frac{\pi}{a}(\zeta-\zeta_{\mathrm{v}}) - \log\sin\frac{\pi}{a}(\zeta-(\tfrac{1}{2}a+\mathbf{j}h)-\zeta_{\mathrm{v}})\right].$$

Altering this potential for a Kármán vortex street inclined from the real axis at an angle α yields

$$F_{\mathrm{K}_\alpha}(\zeta) = \mathbf{j}\frac{\gamma}{2\pi}\left[\log\sin\left(\frac{\pi}{a}(\zeta-\zeta_{\mathrm{v}})e^{-\mathbf{j}\alpha}\right) - \log\sin\left(\frac{\pi}{a}\left((\zeta-\zeta_{\mathrm{v}})e^{-\mathbf{j}\alpha} - (\tfrac{1}{2}a+\mathbf{j}h)\right)\right)\right]. \tag{3}$$

Potential (3) produces singularities (vortices) at $\zeta = \zeta_{\mathrm{v}} + Nae^{\mathbf{j}\alpha}$ and $\zeta = \zeta_{\mathrm{v}} + Nae^{\mathbf{j}\alpha} + (\frac{1}{2}a+\mathbf{j}h)e^{\mathbf{j}\alpha}$, where $N = 0, \pm1, \pm2, \ldots$.

Next, add the potential for a lifting cylinder (1) to the potential for a Kármán vortex street (3) to obtain the potential of a cylinder in a vortex street. To maintain the lifting cylinder as a boundary in the flow, $F_{\mathrm{K}_\alpha}(\zeta)$ must be altered with the Milne-Thomson Circle Theorem‡ [33],

$$w(z) = f(z) + \overline{f}\left(\frac{r_0^2}{z}\right), \tag{4}$$

which allows any potential flow $f(z)$ to be augmented to include a cylinder of arbitrary radius r_0 placed at the origin of the coordinate system. As will be shown in Section 2.2, we impose a cylindrical boundary condition at an arbitrary center, not the origin. (A thorough proof of the Circle Theorem can be found in [35, Section 2.1].) The key to the proof of (4) is that for a point z on a circle C centered at the origin with radius r_0, the complex conjugate is $\overline{z} = r_0^2/z$. To derive the Circle Theorem about an off-origin cylinder, we need only to find the complex conjugate of a point on a circle centered at z_0, which can be shown by substitution to be $\overline{z} = r_0^2/(z-z_0) + \overline{z_0}$. The Circle Theorem then becomes

$$w(z) = f(z) + \overline{f}\left(\frac{r_0^2}{z-z_0} + \overline{z_0}\right). \tag{5}$$

(An alternate derivation of the off-origin Circle Theorem using stream functions can be found in [24, Corollary 1].)

Applying (5) to the Kármán vortex street complex potential (3) yields

$$\begin{aligned} F_{\mathrm{K}^\circ_\alpha}(\zeta) = \mathbf{j}\frac{\gamma}{2\pi}\Bigg[&\log\sin\left(\frac{\pi}{a}(\zeta-\zeta_{\mathrm{v}})e^{-\mathbf{j}\alpha}\right) \\ &- \log\sin\left(\frac{\pi}{a}\left(\frac{r_0^2}{\zeta-\zeta_0} + \overline{\zeta_0} - \overline{\zeta_{\mathrm{v}}}\right)e^{\mathbf{j}\alpha}\right) \\ &- \log\sin\left(\frac{\pi}{a}\left((\zeta-\zeta_{\mathrm{v}})e^{-\mathbf{j}\alpha} - (\tfrac{1}{2}a+\mathbf{j}h)\right)\right) \\ &+ \log\sin\left(\frac{\pi}{a}\left(\left(\frac{r_0^2}{\zeta-\zeta_0} + \overline{\zeta_0} - \overline{\zeta_{\mathrm{v}}}\right)e^{\mathbf{j}\alpha} - (\tfrac{1}{2}a-\mathbf{j}h)\right)\right)\Bigg], \end{aligned} \tag{6}$$

where r_0 is the radius of a cylinder centered at ζ_0 as in (1), ζ_{v} is the location of the primary vortex in the Kármán vortex street, and γ is the vortex strength. This complex potential represents the flow field of a Kármán vortex street augmented to include the lifting cylinder (which will be transformed to become an airfoil) as a streamline of the flow. The conjugate velocity field is

$$\frac{\mathrm{d}F_{\mathrm{K}^\circ_\alpha}}{\mathrm{d}\zeta} = \mathbf{j}\frac{\gamma}{2a}\left[\cot\left(\frac{\pi}{a}(\zeta-\zeta_{\mathrm{v}})e^{-\mathbf{j}\alpha}\right)e^{-\mathbf{j}\alpha}\right.$$

‡ Here the overline operator in $\overline{f}(\cdot)$ indicates that $\mathbf{j}$ is replaced by $-\mathbf{j}$ everywhere it appears in $f(\cdot)$. Note that this is not the same as taking the conjugate of the result, $\overline{f(\cdot)}$, or evaluating the function with the conjugate of the argument, $f(\bar{\cdot})$. However, it is true that $\overline{f}(\cdot) = \overline{f(\bar{\cdot})}$.

$$
\begin{aligned}
&- \cot\left(\frac{\pi}{a}\left(\frac{r_0^2}{\zeta-\zeta_0}+\overline{\zeta_0}-\overline{\zeta_\mathrm{v}}\right)e^{\mathbf{j}\alpha}\right)e^{\mathbf{j}\alpha} \qquad (7)\\
&- \cot\left(\frac{\pi}{a}\left((\zeta-\zeta_\mathrm{v})e^{-\mathbf{j}\alpha}-(\frac{1}{2}a+\mathbf{j}h)\right)\right)e^{-\mathbf{j}\alpha}\\
&+ \cot\left(\frac{\pi}{a}\left(\left(\frac{r_0^2}{\zeta-\zeta_0}+\overline{\zeta_0}-\overline{\zeta_\mathrm{v}}\right)e^{\mathbf{j}\alpha}-(\frac{1}{2}a-\mathbf{j}h)\right)\right)e^{\mathbf{j}\alpha}\Bigg].
\end{aligned}
$$

Adding (1) and (6) yields the total potential flow of a lifting cylinder in the flow field of a Kármán vortex street.

$$F_\mathrm{T}(\zeta) = F_\mathrm{C}(\zeta) + F_{\mathrm{K}_\alpha^\circ}(\zeta). \qquad (8)$$

Similarly, adding (2) and (7) yields total conjugate velocity

$$W_\mathrm{T}(\zeta) = \frac{\mathrm{d}F(\zeta)}{\mathrm{d}\zeta} = \frac{\mathrm{d}F_\mathrm{C}(\zeta)}{\mathrm{d}\zeta} + \frac{\mathrm{d}F_{\mathrm{K}_\alpha^\circ}(\zeta)}{\mathrm{d}\zeta}. \qquad (9)$$

A simulation of this flow field in the pre-transform ζ-plane can be seen in Figure 2(a).

2.2. Flow in the z-plane

The Joukowski transformation allows the potential flow over a cylinder to be used in order to calculate the flow over an airfoil, the parameters of which are chosen to resemble the cross-section of a fish. The transformation is given by [10]

$$z(\zeta) = \zeta + \frac{c^2}{\zeta}, \qquad (10)$$

where $c = \ell/4$ is the quarter-chord length and ℓ is the chord length (the length of the fish-shaped body). The center ζ_0 and radius r_0 of the cylinder in the ζ-plane determine the geometry of the airfoil produced by the Joukowski transformation. The center and radius are [10]

$$\zeta_0 = c\left(\frac{-4}{3\sqrt{3}}\frac{t_\mathrm{a}}{\ell} + 2\mathbf{j}\frac{h_\mathrm{a}}{\ell}\right) \qquad (11)$$

$$r_0 = \left(\frac{\ell}{4} + \frac{t_\mathrm{a}}{3\sqrt{3}}\right), \qquad (12)$$

where h_a is the max height of the camber line from the chord line and t_a is the max thickness of the airfoil. For this work we use an inflexible and uncambered airfoil, so $h_\mathrm{a} = 0$.

The conjugate velocity at a point z in the z-plane is found using the derivative of the Joukowski transformation [10], i.e.,

$$
\begin{aligned}
W(z) = \frac{\mathrm{d}F_\mathrm{T}}{d\zeta}\frac{\mathrm{d}\zeta}{dz} &= \frac{\mathrm{d}F_\mathrm{T}}{\mathrm{d}\zeta}\left(\frac{\mathrm{d}z}{\mathrm{d}\zeta}\right)^{-1}\\
&= W_\mathrm{T}(\zeta(z))\left(1-\left(\frac{c}{\zeta(z)}\right)^2\right)^{-1} \qquad (13)\\
&= u(z) - \mathbf{j}v(z).
\end{aligned}
$$

To find the velocity around the airfoil at point z, (13) must be evaluated at the corresponding point in the ζ-plane by the inverse Joukowski transformation [36]

$$\zeta(z) = \frac{1}{2}\left(z + \mathrm{sgn}\left(\Re(z)\right)\sqrt{z^2-4r_0^2}\right). \qquad (14)$$

A simulation of this flow field in the post-transform z-plane is in Figure 2(b). The z-plane is the physical plane, whereas the ζ-plane is a convenient, non-physical space used to perform calculations. Note that since the vortex street model is defined in the ζ-plane, vortices are deviated slightly from the intended pattern in the z-plane after the Joukowski transformation. However, the error in vortex location due to the transformation will not exceed $r_0 - t_\mathrm{a}/2$, the maximum distance a point on the cylinder's surface is displaced by the Joukowski transformation.

The circulation of the lifting cylinder Γ_C in (1) remains a free parameter, but can be prescribed by the Kutta condition [10]. In this context, the Kutta condition states that the trailing edge of the airfoil must be a stagnation point in order to avoid non-physical infinite velocities around the sharp trailing edge [10]. Through the Joukowski transformation, the trailing edge of the airfoil corresponds to the point in the ζ-plane where the cylinder intersects the real axis. The angle from the center of the cylinder to the trailing edge point is $\theta_0 = -\alpha - 2h_\mathrm{a}/\ell$ [10]. To solve for Γ_C, we must find the tangential and radial components of the velocity with respect to the center of the cylinder and solve for the circulation that results in a stagnation point at the trailing edge. Changing to polar coordinates centered on the cylinder by substituting $\zeta = \zeta_0 + re^{\mathbf{j}\theta}$ into (9) yields

$$\tilde{W}_\mathrm{T}(r,\theta) = W_\mathrm{T}(\zeta) = W_\mathrm{T}(\zeta_0 + re^{\mathbf{j}\theta}).$$

The radial u_r and tangential u_θ components of a complex velocity are [10]

$$u_r(r,\theta) - \mathbf{j}u_\theta(r,\theta) = \tilde{W}_\mathrm{T}(r,\theta)e^{\mathbf{j}\theta},$$

which implies

$$
\begin{aligned}
u_r &= \Re\left(\tilde{W}_\mathrm{T}(r,\theta)e^{\mathbf{j}\theta}\right) \qquad (15)\\
u_\theta &= -\Im\left(\tilde{W}_\mathrm{T}(r,\theta)e^{\mathbf{j}\theta}\right).
\end{aligned}
$$

Substituting $r = r_0$ and $\theta = \theta_0 = -\alpha - 2h_\mathrm{a}/\ell$ in (15), u_r evaluates to 0 as expected, because the cylinder was chosen to be a boundary in the flow. Setting $u_\theta = 0$ and solving for Γ_C yields the circulation that satisfies the Kutta condition (see Appendix A).

2.3. Pressure measurement equation

Bernoulli's equation combined with the flow velocities modeled above predicts the pressure at a point z in the flow field of a Joukowski foil in a vortex street. Let $p(z)$ denote the static pressure at z, ρ the fluid density,

$W(z)$ the velocity at z, g the gravitational acceleration, and Z the elevation. Applying Bernoulli's principle [11] for steady, inviscid, incompressible, irrotational flow yields

$$p(z) + \frac{1}{2}\rho|W(z)|^2 + \rho g Z = \text{constant}. \tag{16}$$

In the experiment described in Section 6, four pressure sensors are mounted on the body of the Joukowski foil. Inspired by the function of canal neuromasts [37], pressure differences between sensors are measured and modeled to remove the effects of ambient pressure, rather than using the absolute pressure measurements. From (16), for any two sensor locations z_i and z_j, we have

$$p(z_i) + \frac{1}{2}\rho|W(z_i)|^2 = p(z_j) + \frac{1}{2}\rho|W(z_j)|^2.$$

The pressure difference, $\Delta p_{ij} = p(z_i) - p(z_j)$, is

$$\Delta p_{ij} = \frac{1}{2}\rho\Big[|W(z_j)|^2 - |W(z_i)|^2\Big], \tag{17}$$

where $W(z)$ is given by (13).

3. Vortex street estimation

The estimation of the states of the vortex street is performed by a recursive, grid-based Bayesian filter [38, 39]. The principle of this filter is to form a measurement model that predicts what the measurements from the sensors would be if the state of the system were a particular value in the state space. By comparing the measurement predictions of every point in the state space grid with the actual measurement, a multi-dimensional conditional probability density function (PDF) is formed, called the measurement likelihood function. The likelihood function is combined with the *prior* PDF of the previous time step to become the *posterior* PDF according to Bayes' theorem. The posterior then becomes the prior of the next time step after it is forecast forward according to the system dynamics including process noise.

In our framework, the Bayesian filter assimilates pressure difference measurements to estimate the strength, phase, and cross-stream location of the vortex street. Equations (9), (13), and (17) are used in Section 2 to model pressure measurements from the sensors. The recursive, grid-based Bayesian filter estimates a set $\mathbf{X}$ of parameters from a set $\mathbf{Y}$ of measurements [38]. Suppose the instantaneous measurement vector is

$$\mathbf{Y} = \mathscr{H}(\mathbf{X}) + \eta, \tag{18}$$

where $\mathscr{H}(\mathbf{X})$ is the (nonlinear) measurement equation (17) and η is (Gaussian) sensor noise. With n_{ps} pressure sensors, there are $n_p = n_{ps} - 1$ measurements of linearly independent pressure differences. Note that there are $n_p = (n_{ps}^2 - n_{ps})/2$ total pressure differences among the pressure sensors, but they are not linearly independent. Using redundant pressure sensor differences in the Bayesian filter framework will have the effect of mitigating sensor noise more quickly (in fewer time steps), but each time step will take longer. In this work, we use the minimum number of linearly independent sensors in order to have the maximum update rate to accomodate the real time dynamics of the Joukowski foil under closed-loop control. The measurement vector is

$$\mathbf{Y} = [\Delta p_1, \ \ldots \ , \Delta p_{n_p}]^T \in \mathbb{R}^{n_p}, \tag{19}$$

where each pressure difference entry is given by (17) evaluated using the locations of the pressure sensors in frame $\mathcal{B}$.

For the grid-based Bayesian filter with Gaussian measurement noise, the likelihood function is the following conditional probability of measurement $\mathbf{Y}$ given state vector $\mathbf{X}$ [38]:

$$\pi(\mathbf{Y}|\mathbf{X}) = \frac{1}{\sqrt{(2\pi)^n \det(R)}} \exp\left[-\frac{1}{2}(\mathbf{Y} - \mathscr{H}(\mathbf{X}))^T R^{-1}(\mathbf{Y} - \mathscr{H}(\mathbf{X}))\right], \tag{20}$$

where n is the dimension of the state space and $R \in \mathbb{R}^{n_p \times n_p}$ is the covariance matrix of the sensor noise. Let m_i be the width of the i^{th} dimension in the n-dimensional state space, then the discrete grid $\mathbf{X} \in \mathbb{R}^{m_1 \times m_2 \times \ldots \times m_n}$ of all expected possible values of the state space is used to evaluate the measurement equation. (For a large number of grid points, this calculation may be computationally intensive.)

Bayes' formula allows each new measurement and its likelihood function (20) to be combined with the prior estimate, yielding the posterior estimate. Let $\mathbf{Y}_k$ be the set of measurements at time t_k, with $k = 1, 2, \ldots$. Then,

$$\pi(\mathbf{X}|\mathbf{Y}_k, \ldots, \mathbf{Y}_1) = \kappa\pi(\mathbf{Y}_k|\mathbf{X})\pi(\mathbf{X}|\mathbf{Y}_{k-1}, \ldots, \mathbf{Y}_1),$$

where κ is a normalizing factor to ensure the posterior integrates to one. After the incorporation of each new measurement, the posterior becomes the prior for the next time step. For the initial time step, we choose a uniform prior. The notation $\pi(\mathbf{X}|\mathbf{Y})$ is used for the posterior $\pi(\mathbf{X}|\mathbf{Y}_k, \ldots, \mathbf{Y}_1)$ at an arbitrary value of k.

The posterior estimate $\pi(\mathbf{X}|\mathbf{Y})$ is an n-dimensional matrix with each dimension corresponding to one of the states in the parameter space. The width m_i of each dimension is determined by how fine a grid is chosen for the Bayesian filter. The computational time needed for each time step increases with the size of $\pi(\mathbf{X}|\mathbf{Y})$. The time evolution of the posterior (in order to become the prior of the next time step) is accomplished by shifting the values of the PDF according to the continuous dynamics of Section 4. The angle of

attack α is a known input and is assumed constant over each time step, allowing each point in the posterior to be forecast using a numerical solver such as `ode45` in MATLAB.

Process noise is modeled by convolving the PDF with an n-dimensional, zero-mean Gaussian kernel as a numerical approximation of the Fokker-Planck equation with diffusion only [40]. This operation has a blurring effect on the PDF as time goes on. In the absence of new measurements, the PDF becomes uniform as time goes to infinity.

The full flow field given in (13) is determined by the geometry of the Joukowski airfoil, the circulation of the airfoil found by the Kutta condition in (A.1), and the parameters of the Kármán vortex street. Each parameter to be estimated in the Bayesian filter framework greatly increases the computational time needed at each time step. It is therefore advantageous to reduce the number of parameters in the estimation state space as much as possible. For example, the geometry of the foil is known by design and Γ_{C} is a function of the other states of the system.

There are seven parameters that uniquely determine the flow field: U (the freestream flow speed), α (the angle of attack of the airfoil), γ (the strength of each vortex in the street), a (the horizontal spacing of the vortices), h (the vertical spacing of the vortices), x_{v} (the horizontal location of the vortex street in frame $\mathcal{A}$), and y_{v} (the vertical location of the vortex street in frame $\mathcal{A}$). Previous work [6] demonstrated the use of pressure sensors to estimate the free-stream speed of a flow as well as the angle of attack. Thus, assume here that flow speed U and angle of attack α are estimated by an independent, parallel filter.

The stability analysis in [8] shows that the vertical spacing h of the vortices is directly proportional to the horizontal spacing a by $h = a\frac{1}{\pi}\sinh^{-1}(1) \approx 0.2805a$, so h can be removed from the parameter space. The horizontal spacing a is related to the diameter of the upstream obstacle shedding the vortices through the Strouhal number St. For low-frequency vortex shedding [41],

$$St = \frac{fD}{U} \approx 0.2, \tag{21}$$

where f is the frequency of shedding, D is the obstacle diameter, and U is the flow speed. The frequency obeys $f = U/a$, so if the obstacle diameter is known, then a may be calculated. Finally, because $x_{\mathrm{v}} = \Re(z_{\mathrm{v}})$ measures the horizontal distance to the closest anti-clockwise vortex in an infinite line of vortices moving at constant speed U, this distance is represented by a phase angle

$$\phi = 2\pi\frac{x_{\mathrm{v}}}{a},\ \phi \in [-\pi,\, \pi). \tag{22}$$

A phase angle of $\phi = 0$ corresponds to when the primary vortex is horizontally in line with the Joukowski foil; $\phi = \pi$ is when the primary vortex is at $x_{\mathrm{v}} = a/2$ and a new vortex becomes the primary vortex. In this way, the parameter space is reduced to three variables: ϕ (the phase of the vortex street), y_{v} (the cross-stream distance to the primary vortex of the street), and γ (the strength of the street). Though only the phase and cross-stream distance are necessary for the controller described in Section 4, the vortex strength must be estimated to have the full mathematical description of the vortex state that is necessary for the Bayesian filter. For the Kármán vortex street, the grid of all possible values is three-dimensional with $\mathbf{X}_{\mathrm{K}^\circ_\alpha} \in \mathbb{R}^{m_\phi \times m_{y_{\mathrm{v}}} \times m_\gamma}$.

The sensor noise matrix in (20) is

$$R = \mathrm{diag}(\underbrace{R_p \ \ldots \ R_p}_{n_p}),$$

where R_p is the expected noise variance of the pressure-difference measurements, found by fitting a Gaussian density to the data collected from the pressure sensors in uniform flow.

4. Dynamics and flow-relative control

To design a controller, perform the observability analysis of Section 5, and perform the forecast step of the Bayesian filter, a model of the system dynamics is needed. We make several assumptions about the dynamics of the Joukowski foil and vortices. The first is that the effect of the vortex street on the Joukowski foil is ignored. In order to account for these dynamics, the lift L in the $\mathbf{a}_1$ direction (see Figure 1) would be given by the Kutta-Joukowski Theorem [10] as $L = \rho U \Gamma_{\mathrm{C}}$, where Γ_{C} from (A.1) is a function of angle of attack α. In the absence of a vortex street, i.e., in a uniform flow, this lifting law reduces to the thin airfoil theory below.

The second assumption is that the airfoil does not affect the path of the vortices in the street. Each vortex in the street deflects from its nominally straight path as it interacts with the obstruction of the airfoil. This effect is well modeled in potential flow using Routh's Rule [42, 43], but individual movement of vortices in the vortex street is not represented in our framework because the measurement equation (17) assumes the entire vortex street can be represented by one set of planar coordinates. The error due to this effect is mitigated because the vortices are only deflected once they are downstream of the airfoil. Previous work [36] has shown that the most effective sensor placement is near the head of the Joukowski foil and is thus less effected by the vortex deflection than if the sensors were placed closer to the tail. The third assumption is that the vortices are constant strength and do not decay as they move downstream.

For the cross-stream coordinate y_v dynamics, we adopt the lifting law from thin airfoil theory [11]. Thin airfoil theory shows that the sectional lift coefficient $c_l = 2\pi\alpha$ and

$$L = c_l q S = \rho\pi U^2 S\alpha, \tag{23}$$

where S is the surface area of the foil. We model the cross-stream dynamics as

$$m\ddot{y}_\mathrm{v} = -L - b\dot{y}_\mathrm{v}, \tag{24}$$

where b is a damping term and the negative sign on L is included because y_v measures the vertical displacement of the primary vortex relative to the center of the foil. If the Joukowski foil has positive lift, y_v decreases as the foil moves in the positive $\mathbf{a}_2$ direction.

Because the Joukowski foil is fixed in the downstream direction, the phase angle ϕ (which keeps track of the $\mathbf{a}_1$ coordinate, x_v, according to (22)) is unaffected by the foil's movement and the vortices advect in the flow at speed U. The downstream dynamics are

$$\dot{\phi} = 2\pi\frac{U}{a} = \text{constant}. \tag{25}$$

Finally, the vortex strength dynamics are

$$\dot{\gamma} = 0,$$

because of the assumption that the vortices do not decay as they travel downstream.

For our Kármán vortex street setting, the goal of the closed-loop control is to track a phase-dependent reference trajectory $y_\mathrm{v,ref} = y_\mathrm{v,ref}(\phi)$, meaning for any given phase ϕ there is a reference vertical position y_v that should be achieved by actuating the angle of attack α of the Joukowski foil. Note that y_v is the position of the vortex street in body-fixed, non-rotating frame $\mathcal{A}$ (see Figure 1) so if the Joukowski foil moves in the $\mathbf{e_2}$ direction in the inertial frame $\mathcal{I}$, y_v decreases. All calculations within the estimator and controller are performed in body-fixed frame $\mathcal{B}$. If the Kármán vortex street never moves in the cross-stream direction, y_v still changes if the Joukowski foil translates in the cross-stream direction.

Let $\hat{\phi}$ and $\hat{y}_\mathrm{v}$ represent the maximum likelihood estimate of the relative phase and cross-stream position of the vortex street from $\pi(\mathbf{X}|\mathbf{Y})$, the three-dimensional PDF output every time step by the Bayesian filter (see Section 3). Although the posterior is only updated once per time step, the relatively fast update rate of 20 Hz allows the system to be well characterized by continuous dynamics. The reference trajectory $y_\mathrm{v,ref} = y_\mathrm{v,ref}(\hat{\phi})$ is a function of the estimate of the phase of the vortex street. Letting $e_1 = \hat{y}_\mathrm{v} - y_\mathrm{v,ref}$ and $e_2 = \dot{\hat{y}}_\mathrm{v} - \dot{y}_\mathrm{v,ref}$, the error dynamics are

$$\dot{e}_1 = e_2$$
$$\dot{e}_2 = -\frac{1}{m}\rho\pi U^2 S\alpha - \frac{b}{m}\dot{\hat{y}}_\mathrm{v} - \ddot{y}_\mathrm{v,ref},$$

where the cross-stream dynamics (23) and (24) have been used. We choose a tracking PD controller [44] for the angle of attack α,

$$\alpha = -\frac{m}{\rho U^2\pi S}\left(\ddot{y}_\mathrm{v,ref} + \frac{b}{m}\dot{\hat{y}}_\mathrm{v} - k_p e_1 - k_d e_2\right), \tag{26}$$

with control gains $k_p = k_d = 5$. Damping constant $b = 15\,\mathrm{kg\,s^{-1}}$ was found to best match the experimental dynamics through trial and error. This damping term represents the damping effect of the water on the Joukowski foil as well as the nonzero friction of the air-bearing system. The stable, closed-loop error dynamics are

$$\dot{e}_1 = e_2$$
$$\dot{e}_2 = -k_p e_1 - k_d e_2,$$

with eigenvalues of

$$\lambda = -\frac{k_d}{2} \pm \frac{\sqrt{k_d^2 - 4k_p}}{2},$$

which have negative real parts since $k_p, k_d > 0$.

5. Observability-based path-planning

The observability of a system quantifies the capability of a set of outputs $\mathbf{Y}$ to be used to infer the internal states $\mathbf{X}$ of the system on which the outputs depend. We use this concept here to find the reference trajectory through the vortex street that leads to the best estimates of the street parameters. Traditional observability gives a binary answer to the question of whether measurements $\mathbf{Y}$ can be used to estimate states $\mathbf{X}$ and, for nonlinear systems such as ours, often requires taking Lie derivatives of the system dynamics and evaluating the observability rank condition [45]. Empirical observability instead gives a quantatative measure of how easily observed a system is and requires only the ability to simulate the system dynamics. Krener and Ide conceived the *empirical observability gramian* W_o [45]. For the nonlinear system

$$\dot{\mathbf{X}} = f(t, \mathbf{X}) \text{ and } \mathbf{Y} = \mathscr{H}(t, \mathbf{X}),$$

$$W_o(i,j) = \frac{1}{4\epsilon^2}\int_0^\tau (\mathbf{Y}^{+i} - \mathbf{Y}^{-i})^\top (\mathbf{Y}^{+j} - \mathbf{Y}^{+j})\mathrm{d}t, \tag{27}$$

where $\mathbf{Y}^{\pm i}$ is the measurement produced from the state $\mathbf{X}^{\pm i} = \mathbf{X} \pm \epsilon\mathbf{e}^i$, and $\epsilon\mathbf{e}^i$ is a small perturbation along the i^{th} unit vector in $\mathbb{R}^n$, with $i = 1, \ldots, n$. The inverse of the minimum singular value of W_o on a time interval $[0, \tau]$ is the *local unobservability index*, $\nu = 1/\sigma_{\min}(W_o)$. Since this metric requires simulating the system dynamics, it depends on parameters specific to experimental conditions such as sensor placement, vortex strength, foil geometry, etc., and therefore cannot be used to compare observability between different configurations. It is, however, useful

for comparing different trajectories with the same experimental configuration. The path with the lowest unobservability index will lead to the best estimate of the parameter space.

To choose the path $y_{\mathrm{v,ref}}(\phi)$, the unobservability indices ν calculated along sinusoidal trajectories of varying phase and amplitude are compared. We examine sinusoidal trajectories because of the repeating structure of the vortex street and the sinusoidal nature of Kármán gaiting behavior in fish. By simulating the system dynamics given in Section 4 with the control law for α described therein, (27) provides the local unobservability index for each trajectory. Nominal initial conditions are set to start on the reference trajectory. The street spacing, vortex strength, flow speed, foil geometry, and sensor configuration match those in the experiment described in Section 6. Figure 3(a) shows the local unobservabiltiy index for each sinusoidal reference trajectory. The minima on this graph indicated by white circles are the paths of the Joukowski foil leading to the best estimates of the parameters $\mathbf{X}_{\mathrm{K}^\circ_\alpha}$.

The corresponding optimal paths are shown in Figure 3(b) in white. Figure 3(b) was generated not by simulating full trajectories with the proper control law, but by selecting initial conditions in the (ϕ, y_{v}) plane and simulating the dynamics with $\alpha = 0$ for one time step of 0.1 seconds. Figure 3(b) gives a metric for the unobservability for each point in the plane regardless of how that point was reached, referred to here as the short-term unobservability index. In contrast, Figure 3(a) gives a metric for the unobservability of an entire reference trajectory, referred to here as the long-term unobservability index. Each point in Figure 3(a) corresponds to an entire trajectory through Figure 3(b). The low unobservability index areas in Figure 3(b) are those that bring one of the four pressure sensors close to a vortex in the street. The optimally observable paths shown in white are those that bring the vortices close to these low unobservability index areas, creating a large pressure difference among the sensor pairs and hence a good estimate of the parameters.

For the experimental demonstration described in Section 6, the black trajectory was chosen for $y_{\mathrm{v,ref}}$ for three reasons. First, it avoids unmodeled boundary effects of coming too close to the walls of the test section (indicated by black dashed lines). Second, the sensors do not pass directly through the singularity of the vortices as they do for the white trajectories. In the potential flow model, the velocity at the center of each vortex is infinite, which is of course nonphysical, so by avoiding intentional measurements at the singularities, we avoid a discrepancy between the model and the real world. Finally, it is very close to the two white

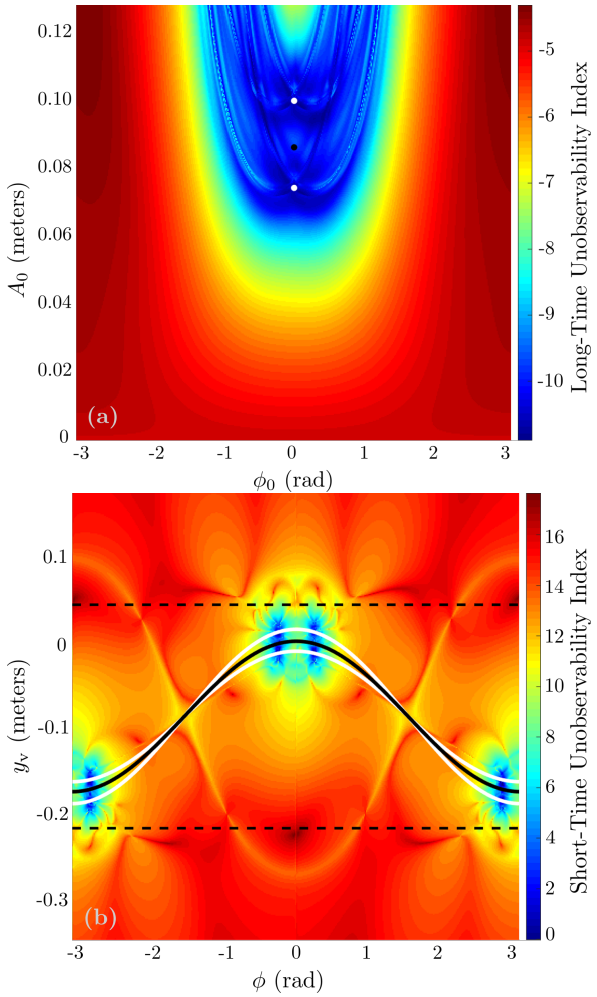

Figure 3. (a) Long-time unobservability index for sinusoidal trajectories of the form $A_0\cos(\phi+\phi_0) - h/2$ through the (ϕ, y_{v}) plane. White circles represent minima of the test grid. Black circles represent the path followed in the experiment. (b) Short-time unobservability index at various points in the (ϕ, y_{v}) plane. White and black curves correspond to the white and black circles in (a). The dashed black lines indicate the width of the test section of the experimental setup described in Section 6.

trajectories and has a low unobservability index as compared to the rest of the field in Figure 3(a). The chosen path is

$$y_{\mathrm{v,ref1}} = \frac{h}{2}\cos(\phi) - \frac{h}{2}, \tag{28}$$

which takes the center of the Joukowski foil (but not the pressure sensors) through the center of each vortex. The offset $-h/2$ ensures that the trajectory is centered between the upper and lower lines of vortices in the street. It is interesting to note that fish do not adopt this strategy. Instead, they slalom between the vortices capturing some of the energy to propel themselves [12], a behavior known as Kármán gaiting. To demonstrate this path, a second reference trajectory is defined as

$$y_{\mathrm{v,ref2}} = \frac{h}{2}\cos(\phi+\pi) - \frac{h}{2}, \tag{29}$$

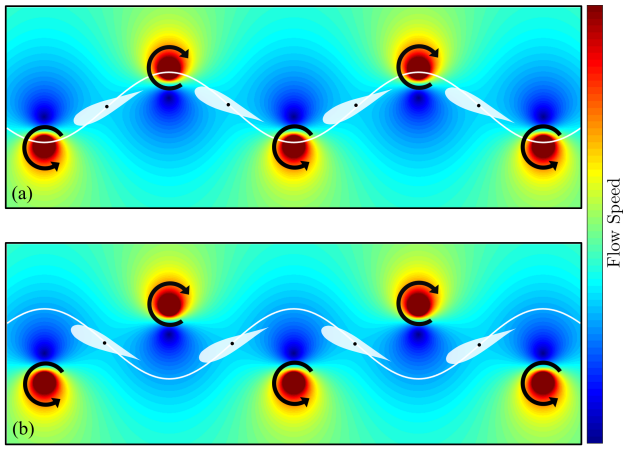

Figure 4. (a) Reference trajectory 1, the optimally observable path through the vortex street. The Joukowski foil passes through each vortex in the street. (b) Reference trajectory 2, the slalom path corresponding to Kármán gaiting. Note that this figure is in a flow-fixed frame. In the inertial frame, the Joukowski foil is fixed in the downstream coordinate and the vortices flow past it.

representing the Kármán gaiting behavior.

Figure 4 shows the difference between the two reference trajectories that are executed in the experiments described in Section 6.

6. Experimental demonstration

Figure 5 shows the experimental testbed for the Kármán vortex street. A 185 L Loligo flow tank creates a uniform 15 cm/s flow in an 88cm × 25cm × 25cm test section. A stepper motor controls a black acrylic fin that flaps to create vortices at the desired spacing and frequency. The fin extends to the bottom of the flow tank and is parallel to the flow until a vortex is generated. The fin then rotates clockwise (anti-clockwise) and slowly returns to center to create an anti-clockwise (clockwise) vortex that travels downstream with the flow. This pattern is consistent with that of a Kármán vortex street shed from an obstacle in the flow (rather than a reverse Kármán vortex street which is found in the wake of swimming fish). Through the use of dye packets and image processing, the strength of each vortex in the street was empirically determined to be $\gamma \approx 0.0605\,\mathrm{m^2 s^{-1}}$.

The Joukowski foil is suspended in the water from a servomotor that controls the angle of attack directly according to (26). The servomotor is mounted on a set of nearly frictionless air bearings. The air bearings have a supply of compressed air that is released radially inward towards a 3/4 inch steel shaft, creating a pillow of air that supports the air bearings as they move. This configuration allows the servomotor and

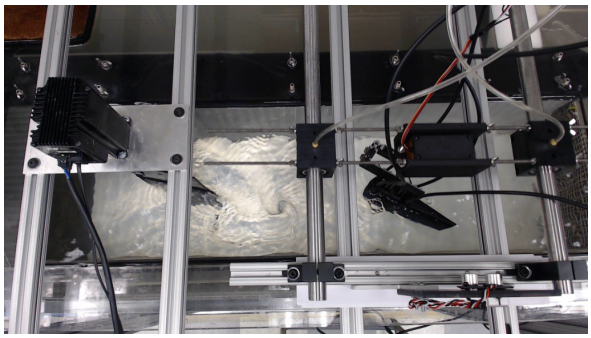

Figure 5. The experimental testbed for the vortex street. A flow tank generates flow from left to right. The Joukowski foil, equipped with four pressure sensors as an artificial lateral line, controls its cross-stream position by actuating a servomotor to control angle of attack. The Joukowski foil is attached to an air-bearing system that allows free movement in the cross-stream direction, but fixes the foil in its downstream position. A stepper motor actuates a fin to create the vortices in the desired vortex street pattern. An overhead camera is used to to calculate the ground truth location of the vortices.

Joukowski foil to freely translate in the cross-stream direction, but holds the foil locked at a particular downstream position from the vortex generator. Four Millar pressure sensors are mounted directly on the side of the fish body to emulate the lateral line seen in biology. The variance of noise in the pressure sensors was found to be $R_p = 49\ \mathrm{Pa}^2$.

Printed from PLA plastic with a MakerBot Replicator, the rigid Joukowski foil has the shape detailed in Section 2. The print includes internal cutouts to allow an assembly of 1 cm MakerBeam to mount the foil to the servomotor horn. The length of the Joukowski foil is 15 cm and maximum thickness is 2 cm. The body is uncambered. The height of the body (the span of the foil) is 12 cm and was suspended into the water to leave 2 cm exposed to air and to eliminate any unmodeled flow over the top of the foil. Pressure sensors were mounted on the Joukowski foil at the locations shown in Figure 1 and were midway down the depth of the body.

A camera mounted above records the experiments in order for the actual vortex positions to be determined offline. This method relies on the easy visibility of the center of each vortex and therefore does not provide ground truth when the vortices dissipate or are occluded by something in the experimental setup. Particle image velocimetry provides more accurate and robust ground truth data for vortex position, but imaging of this type was precluded here because of the physical properties of the flow tank.

The estimation, data acquisition, image capture, control calculation, stepper motor, and servomotor are all controlled in real time from a laptop computer running MATLAB. A 30×30×15 coarse grid of possible points $\mathbf{X}_{\mathrm{K}^\circ_\alpha}$ in the $(\phi, y_\mathrm{v}, \gamma)$ state space was used to

update the estimate and control at approximately 20 Hz in order to have stable convergence to the reference trajectory. Experiments ran for 700 time steps at 20 Hz, equating to nominally 35 second run times (the actual run time varied by up to 2 seconds due to variable computation time per time step and unknown loads on the computer's processor by programs other than MATLAB). The vortices created by the flapper were spaced by $a = 0.6\,\mathrm{m}$, which corresponds to a hypothetical upstream obstacle of diameter 12 cm according to (21).

Figure 6(a-c) shows the time history of the marginal densities of the three states in $\pi(\mathbf{X}|\mathbf{Y})$ for the closed-loop experiment to track the optimally observable reference trajectory given in (28). The marginal density for each state was formed by summing along the other two states of the three-dimensional probability density at each time step. The initial value of ϕ is plotted instead of the current value for ease of visualization. Integrating (25) directly and rearranging yields

$$\phi_0 = \phi(t) - 2\pi\frac{U}{a}t, \tag{30}$$

the initial value of ϕ. Since this value is constant and the second term is known, a proper estimate of $\phi(t)$ will lead to a constant estimate of ϕ_0. The experiment was successful in actuating the Joukowski foil to pass through each of the vortices after an initial period of larger error. Figure 7(a) shows the time history of the error from the reference trajectory.

Figure 6(d-f) shows the time history of the marginal densities of the three states in $\pi(\mathbf{X}|\mathbf{Y})$ for the closed-loop experiment to track the Kármán gaiting trajectory given in (29). The experiment was successful in actuating the Joukowski foil to slaloming through the vortex street after an initial period of larger error. Figure 7(b) shows the time history of the error from the reference trajectory.

The estimator and controller were successful in both closed-loop control experiments, meaning that there was stable convergence to the reference trajectories and errors tended to zero. For the first five seconds for each experiment, the controller was disabled and the angle of attack was kept at $\alpha = 0$. During this period, the vortices did not come near the pressure sensors on the Joukowski foil and thus the estimate had a very large variance. In both cases, after the controller was enabled, the Joukowski foil came close to the vortices in the street (by design in the optimally observable case and by initial error in the slaloming case) and the variance in the estimate was reduced due to the larger difference in the pressure sensor measurements at this close proximity. This result agrees with the result from the observability analysis in Section 5, which showed that better estimates of the state arise when the fish is close to the vortices. Notice that after the initial five second period, the variance in the estimate of y_v in panel 6(b) (the optimally observable path) is lower than that of panel 6(e) (the Kármán gaiting path) because the latter trajectory does not bring the foil as close to the vortices.

The ground truth values well match the areas of high probability in the estimate, indicating that the estimator is functioning properly. In the last 8 seconds of panel 6(c), the area of highest probability differs from the ground truth by a significant amount. However, the estimate is only one grid-division away from ground truth. A finer grid of possible value of γ may reduce the estimation error, although a finer grid may jeopardize the real time operation.

The estimates of γ and the initial value of ϕ are essentially constant, as expected, because the ground truth values are constant. One exception is in panel 6(a) at around 10 seconds, where the estimate of the initial ϕ increases to the correct value. This increase is accompanied by a decrease in the estimate of γ in 6(c) at the same time, illustrating the deep coupling of the three parameters in the Bayesian filter. A particular measurement may correspond to a vortex very close and weak, or strong and far away. It is through the Bayesian filter's integration of these data through time (new measurements are taken each time step) and space (the distribution of the pressure sensors) that this ambiguity is removed.

The estimates of y_v follow a sinusoidal pattern as expected because the robot is tracking a sinusoidal reference trajectory. The estimator uses the dynamic model presented in Section 4 to shift the probability density at each time step according to the control input it chooses from (26).

7. Conclusion

This paper describes the estimation of vortex flows and its use in closed-loop control of the flow-relative position of a Joukowski foil equipped with distributed pressure sensors inspired by lateral-line neuromasts seen in biology. Measurement equations for these sensors use potential flow theory and Bernoulli's principle. The measurement equations are incorporated in a recursive Bayesian filter to estimate the planar location and strength of the Kármán vortex street. Closed-loop control of the angle of attack of the Joukowski foil successfully actuated its position relative to the vortex street to one of two reference trajectories. The first reference trajectory was an optimal path through the vortex street determined using a metric based on the local unobservability index. The optimally observable trajectory is one that passes

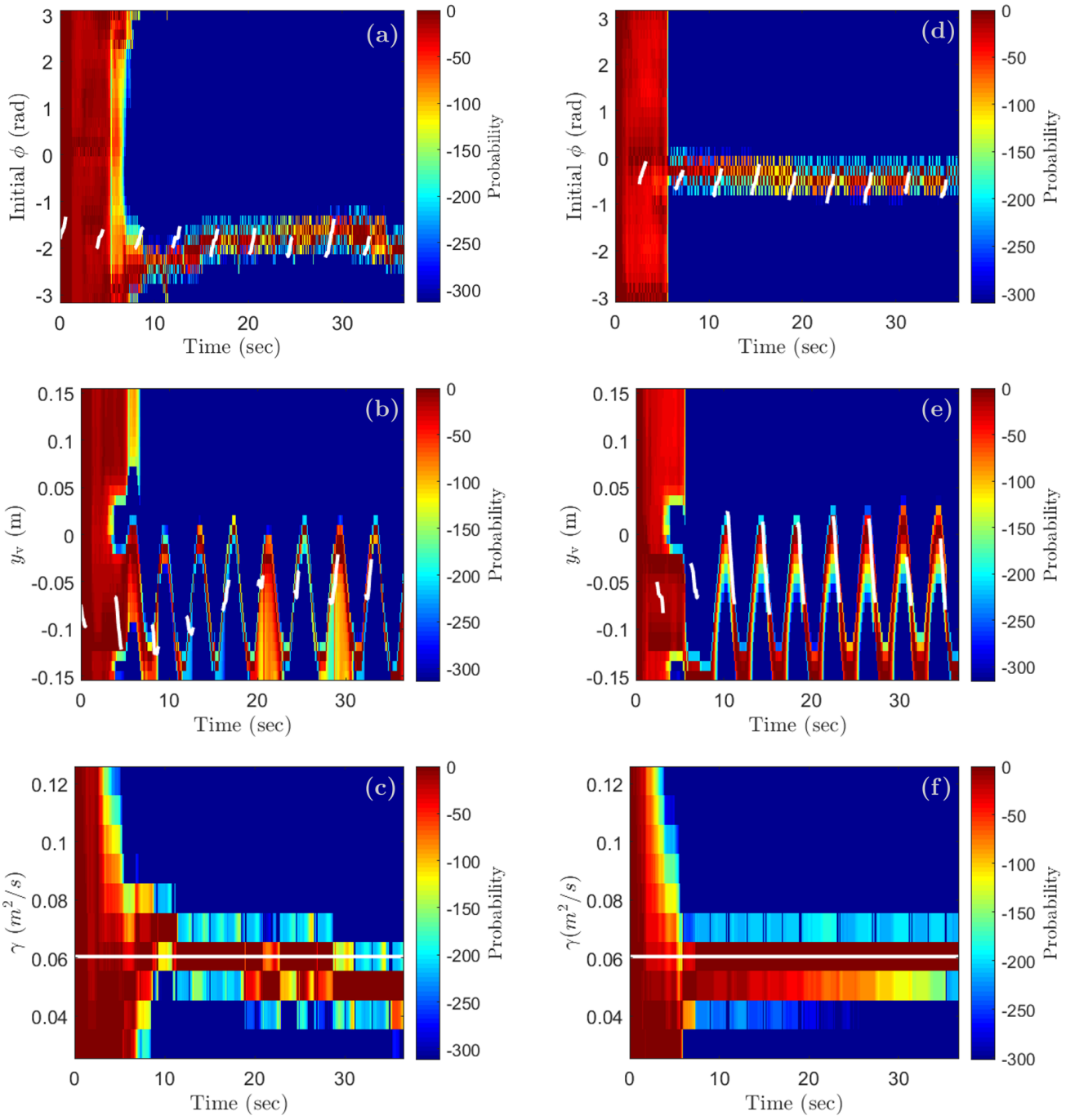

Figure 6. Time history of the marginal posteriors from the Bayesian estimator during the closed-loop control experiment in the flow tank. Panels (a,d) show the initial value of ϕ given by (30), (b,e) y_v, and (c,f) γ. Panels (a-c) correspond to the optimally observable reference trajectory (28) and panels (e-f) correspond to the Kármán gaiting trajectory (29). Feedback control starts at 5 seconds. The white lines indicate the ground truth.

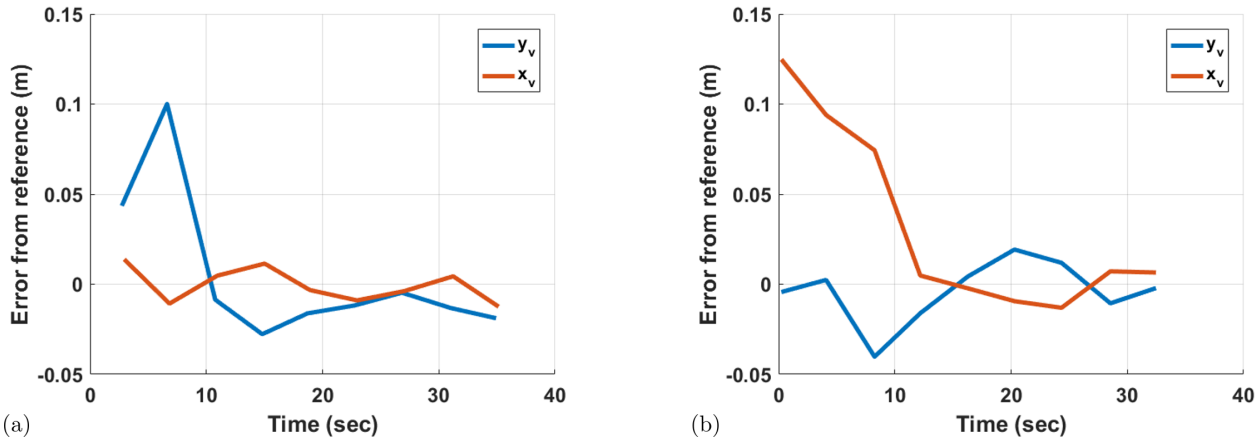

Figure 7. Error between reference and ground truth of x_v and y_v over the Kármán vortex street experiment for the (a) optimal observability and (b) Kármán gaiting trajectory. x_v is shown rather than the non-dimensionalized ϕ to more easily compare the errors in the two states. Feedback control starts at 5 seconds.

through each vortex in the street. The second reference trajectory was inspired by the slaloming trajectory in fish exhibiting Kármán gaiting behavior. The lateral line and Bayesian filter framework were successful in estimating the state of the vortex street and converging to the closed-loop control goal in both cases.

One of the potential applications of this framework is lateral line sensing and feedback control for schooling or pursuit by free-swimming, flexible fish robots. The optimally observable trajectory leads to an estimate with less variance than Kármán gaiting. For a pursuit scenario, tracking the optimally observable trajectory in the wake of swimming fish or robot would give the best estimate of the vortex street and allow the pursuer to follow the tubulent wake upstream to capture the target. However, in a cooperative pursuit or schooling scenario, the Kármán gaiting trajectory may conserve energy. * In cases with large sensor noise, it may be beneficial to begin tracking the optimally observable trajectory to ensure the robot finds the vortex street, and then switch to the more energetically efficient trajectory to conserve energy [13, 32].

In ongoing work, this sensing framework will be adapted for a free-swimming fish robot with a flexible body. A long-term goal is to demonstrate Kármán gaiting behavior in the wake of another fish robot. To locate other fish robots beyond the effective range of the artificial lateral line, the fish robot may be augmented with a computer-vision sensing system.

Acknowledgments

This work is supported in part by the Office of Naval Research under Grant Nos. N000141512246 and N000141612208. Brian Free is also supported by the National Science Foundation Graduate Research Fellowship Program under Grant No. DGE 1322106.

Appendix A.

The circulation of the lifting cylinder as mandated by the Kutta condition is

$$\Gamma_\mathrm{C} = 2r_0\pi\left[\Im\left(\frac{\mathbf{j}\gamma \mathrm{e}^{\mathbf{j}\theta_0}}{2a}(A_1 + A_2 + A_3 - A_4)\right) + 2U\sin(\theta_0)\right], \tag{A.1}$$

where $\theta_0 = -\alpha - h_a/\ell$,

$$A_1 = \mathrm{e}^{\mathbf{j}(\alpha-2\theta_0)}\cot\left[\frac{\pi}{a}\mathrm{e}^{\mathbf{j}\alpha}\left(\overline{\zeta_0} - \overline{\zeta_\mathrm{v}} + r_0\mathrm{e}^{-\mathbf{j}\theta_0}\right)\right],$$

$$A_2 = \mathrm{e}^{-\mathbf{j}\alpha}\cot\left[\frac{\pi}{a}\left(\frac{a}{2} + \mathbf{j}h - \mathrm{e}^{-\mathbf{j}\alpha}\left(\zeta_0 - \zeta_\mathrm{v} + r_0\mathrm{e}^{\mathbf{j}\theta_0}\right)\right)\right],$$

$$A_3 = \mathrm{e}^{-\mathbf{j}\alpha}\cot\left[\frac{\pi}{a}\mathrm{e}^{-\mathbf{j}\alpha}\left(\zeta_0 - \zeta_\mathrm{v} + r_0\mathrm{e}^{\mathbf{j}\theta_0}\right)\right], \text{ and}$$

$$A_4 = \mathrm{e}^{\mathbf{j}(\alpha-2\theta_0)}\cot\left[\frac{\pi}{a}\left(-\frac{a}{2} + \mathbf{j}h + \mathrm{e}^{\mathbf{j}\alpha}\left(\overline{\zeta_0} - \overline{\zeta_\mathrm{v}} + r_0\mathrm{e}^{-\mathbf{j}\theta_0}\right)\right)\right].$$

See Section 2.2 for the derivation.

References

[1] William J. Van Trump and Matthew J. McHenry. The morphology and mechanical sensitivity of lateral line receptors in zebrafish larvae (*Danio rerio*). *The Journal of Experimental Biology*, 211, 2008.

[2] Sheryl Coombs. Signal detection theory, lateral-line excitation patterns and prey capture behaviour of mottled sculpin. *Animal Behavior*, 58(2):421–430, 1999.

[3] Andres Carrillo and Matthew J. McHenry. Zebrafish learn to forage in the dark. *Journal of Experimental Biology*, 219(4):582–589, 2016.

[4] Saurabh Sharma, Sheryl Coombs, Paul Patton, and Theresa Burt de Perera. The function of wall-following behaviors in the Mexican blind cavefish and a sighted relative, the Mexican tetra (*Astyanax*). *Journal of Comparative Physiology*, 195(3):225–240, 2009.

[5] Sheryl Coombs. Smart skins: information processing by lateral line flow sensors. *Autonomous Robots*, 11(3):255–261, 2001.

[6] Francis D. Lagor, Levi DeVries, Kathryn Waychoff, and Derek A. Paley. Bio-inspired flow sensing and control: Autonomous rheotaxis using distributed pressure measurements. *Journal of Unmanned System Technology*, 1(3), 2013.

[7] Brian A. Free, Mukund K. Patnaik, and Derek A. Paley. Observability-based path-planning and flow-relative control of a bioinspired sensor array in a karman vortex street. In *Proc. American Control Conference*, pages 548–554, 2017.

[8] P.G. Saffman. *Vortex Dynamics*. Cambridge University Press, 1992.

[9] Richard Mason. *Fluid Locomotion and Trajectory Planning for Shape-Changing Robots*. PhD thesis, California Institute of Technology, Pasadena, California, 2003.

[10] Ronald L. Panton. *Incompressible Flow*. Wiley, 2005.

[11] John D. Anderson. *Fundamentals of Aerodynamics*. McGraw Hill, 2007.

[12] James C. Liao. The role of the lateral line and vision on body kinematics and hydrodynamic preference of rainbow trout in turbulent flow. *Journal of Experimental Biology*, 209(20):4077–4090, 2006.

[13] James C. Liao. Neuromuscular control of trout swimming in a vortex street: implications for energy economy during the Kármán gait. *Journal of Experimental Biology*, 207(20):3495–3506, 2004.

[14] James C. Liao. A review of fish swimming mechanics and behaviour in altered flows. *Philos. Trans. R. Soc. Lond., B, Biol. Sci.*, 362(1487):1973–1993, Nov 2007.

[15] Brian L. Partridge and Tony J. Pitcher. The sensory basis of fish schools: relative roles of lateral line and vision. *Journal of Comparative Physiology*, 135(4):315–325, 1980.

[16] M.J. McHenry, K.E. Feitl, J.A. Strother, and W.J. Van Trump. Larval zebrafish rapidly sense the water flow of a predator's strike. *Biology Letters*, 5(4):477–479, 2009.

[17] Horst Bleckmann. Reaction time and stimulus frequency in prey localization in the surface-feeding fish *Aplocheilus lineatus*. *Journal of Comparative Physiology*, 140(2):163–172, 1980.

[18] John Montgomery, Sheryl Coombs, and Matthew Halstead. Biology of the mechanosensory lateral line in fishes. *Reviews in Fish Biology and Fisheries*, 5(4):399–416, 1995.

[19] O. Akanyeti, P.J.M. Thornycroft, G.V. Lauder, Y.R. Yanagitsuru, A.N. Peterson, and J.C. Liao. Fish optimize sensing and respiration during undulatory swimming. *Nature Communications*, 7, 2016.

[20] Boris P. Chagnaud, Horst Bleckmann, and Michael H. Hofmann. Kármán vortex street detection by the lateral line. *Journal of Comparative Physiology*, 193(7):753–763, 2007.

[21] Yingchen Yang, Nam Nguyen, Nannan Chen, Michael Lockwood, Craig Tucker, Huan Hu, Horst Bleckmann, Chang Liu, and Douglas L. Jones. Artificial lateral line with biomimetic neuromasts to emulate fish sensing. *Bioinspiration & Biomimetics*, 5(1):016001, 2010.

[22] Amy Gao and Michael Triantafyllou. *Bio-inspired pressure sensing for active yaw control of underwater vehicles*. IEEE, 2012.

[23] Levi DeVries, Frank D. Lagor, Hong Lei, Xiaobo Tan, and Derek A. Paley. Distributed flow estimation and closed-loop control of an underwater vehicle with a multi-modal artificial lateral line. *Bioinspiration & Biomimetics*, 10:1–15, 2015.

[24] Francis D. Lagor, Kayo Ide, and Derek A. Paley. Touring invariant-set boundaries of a two-vortex system using streamline control. In *Proc. IEEE Conference on Decision and Control*, pages 2217–2222, 2015.

[25] Perry Y. Li and Saroj Saimek. Modeling and estimation of hydrodynamic potentials. In *Proc. IEEE Conference on Decision and Control*, volume 4, pages 3253–3258, 1999.

[26] Vicente I. Fernandez. *Performance analysis for lateral-line-inspired sensor arrays*. PhD thesis, Massachusetts Institute of Technology, 2011.

[27] Zheng Ren and Kamran Mohseni. A model of the lateral line of fish for vortex sensing. *Bioinspiration & Biomimetics*, 7(3):036016, 2012.

[28] Taavi Salumäe and Maarja Kruusmaa. Flow-relative control of an underwater robot. In *Proc. R. Soc. A*, volume 469, page 20120671, 2013.

[29] Roberto Venturelli, Otar Akanyeti, Francesco Visentin, Jaas Ježov, Lily D. Chambers, Gert Toming, Jennifer Brown, Maarja Kruusmaa, William M. Megill, and Paolo Fiorini. Hydrodynamic pressure sensing with an artificial lateral line in steady and unsteady flows. *Bioinspiration & Biomimetics*, 7(3):036004, 2012.

[30] Adrian Klein and Horst Bleckmann. Determination of object position, vortex shedding frequency and flow velocity using artificial lateral line canals. *Beilstein Journal of Nanotechnology*, 2:276, 2011.

[31] Wei Wang, Xingxing Zhang, Jianwei Zhao, and Guangming Xie. Sensing the neighboring robot by the artificial lateral line of a bio-inspired robotic fish. In *Intelligent Robots and Systems (IROS)*, pages 1565–1570. IEEE, 2015.

[32] Jaas Ježov, Otar Akanyeti, Lily D Chambers, and Maarja Kruusmaa. Sensing oscillations in unsteady flow for better robotic swimming efficiency. In *Systems, Man, and Cybernetics (SMC)*, pages 91–96. IEEE, 2012.

[33] L.M. Milne-Thomson. *Theoretical Hydrodynamics*. Dover Publications, Inc., 1968.

[34] Peter S. Bernard. *Fluid Dynamics*. Cambridge University Press, 2015.

[35] Serdar Tulu. *Vortex Dynamics in Domains with Boundaries*. PhD thesis, Izmir Institute of Technology, 2011.

[36] Levi DeVries and Derek A. Paley. Observability-based optimization for flow sensing and control of an underwater vehicle in a uniform flowfield. In *Proc. American Control Conference*, pages 1386–1391, 2013.

[37] Branislava Ćurčić-Blake and Sietse M. van Netten. Source location encoding in the fish lateral line canal. *Journal of Experimental Biology*, 209(8):1548–1559, 2006.

[38] M. Sanjeev Arulampalam, Simon Maskell, Neil Gordon, and Tim Clapp. A tutorial on particle filters for online nonlinear/non-Gaussian Bayesian tracking. *IEEE Transactions on Signal Processing*, 50(2):174–188, 2002.

[39] Lawrence D. Stone, Carl A. Barlow, and Thomas L. Corwin. *Bayesian Multiple Target Tracking*. Arctech House, Inc., 1999.

[40] G.W. Wei. A unified approach for the solution of the fokker-planck equation. *Journal of Physics A: Mathematical and General*, 33(27):4935, 2000.

[41] Haniu Sakamoto and H. Haniu. A study on vortex shedding from spheres in a uniform flow. *Journal of Fluids Engineering*, 112(4):386–392, 1990.

[42] Turgut Sarpkaya. Computational methods with vortices-the 1988 freeman scholar lecture. *ASME, Transactions, Journal of Fluids Engineering*, 111:5–52, 1989.

[43] Quen-yaw Sheen. *Potential flow analysis of unsteady Jourkowski airfoil in the presence of discrete vortices*.

PhD thesis, University of Colorado, 1986.

[44] Hassan K. Khalil. *Nonlinear Control*. Pearson, 2015.

[45] Arthur J. Krener and Kayo Ide. Measures of unobservability. In *Proc. IEEE Conference on Decision and Control*, pages 6401–6406. IEEE, 2009.